

NUMERICAL INVESTIGATION OF TURBULENT FLOW AND SCALAR TRANSPORT IN AN INCLINED JET IN CROSSFLOW

J. Bodart

Center for Turbulence Research
Stanford University
488 Escondido Mall, Stanford, CA 94305-3035
jbodart@stanford.edu

F. Coletti

Department of Mechanical Engineering
Stanford University
488 Escondido Mall, Stanford, CA 94305-3035
colettif@stanford.edu

I. Bermejo Moreno

Center for Turbulence Research
Stanford University
488 Escondido Mall, Stanford, CA 94305-3035
ibermejo@stanford.edu

J. K. Eaton

Department of Mechanical Engineering
Stanford University
488 Escondido Mall, Stanford, CA 94305-3035
eaton@stanford.edu

ABSTRACT

An inclined jet in crossflow, characteristic of film cooling applications is studied with highly resolved LES. The configuration reproduces an experimental set-up in which three dimensional measurements of mean velocity and mean flow concentration have been performed using MRV/MRC completed with PIV measurements at some specific locations. The simulations are shown to capture with high fidelity both the separated flow inside the film cooling hole and the distribution of scalar concentration downstream of injection. This paper focuses on the gradient-diffusion hypothesis for the scalar fluxes in RANS modeling. In this configuration we show a large misalignment between turbulent scalar fluxes and the scalar concentration gradient in the streamwise direction.

INTRODUCTION

Film cooling systems induce a range of complex phenomena associated with the interaction of the coolant jet discharging into a crossflow. The jet-in-crossflow configuration has been extensively studied through experiments and direct/large-eddy numerical simulations. However, most of previous simulations consider a laminar crossflow and a transverse jet originating from a fully-developed pipe flow Muppidi & Mahesh (2007). For numerical calculations to capture the physical phenomena relevant to film cooling applications (Acharya *et al.*, 2001), it is necessary to include the effects induced by: (i) the recirculation occurring at the inlet of the short film cooling hole and (ii) the turbulent state of the main flow boundary layer. The first point requires including in the computational domain the plenum feeding the hole. The second condition can be fulfilled by imposing a realistic turbulent flow at the inflow of the developing crossflow. Most previous numerical studies could not afford to satisfy both requirements at the same time (Muldoon & Acharya, 2009; Ziefle & Kleiser, 2008) because of the prohibitive computational cost. In this work a film cooling flow replicating a parallel experimental study by Coletti *et al.* (2012) is investigated by

means of Large Eddy Simulation. A plenum with a quasi-quiet flow is connected to a square duct through a short inclined pipe, injecting a non-buoyant contaminant into the duct flow. Both jet and crossflow are fully turbulent. The measurements are obtained by MRI-based techniques (Benson *et al.*, 2010; Elkins *et al.*, 2003) and include the three-dimensional velocity and concentration fields in the whole physical domain, along with Reynolds stresses measured by PIV along selected planes. The comprehensive experimental database allows a complete validation of the time-averaged calculated fields, also testing the sensitivity of the results to the turbulent Schmidt number employed in the subgrid-scale model.

The simulation, besides achieving higher spatial resolution than the experiments, provides additional information on the turbulent scalar fluxes and on the time-dependent nature of the momentum and scalar transport. The availability of the turbulent scalar fluxes allows the direct evaluation of the turbulent diffusivity and turbulent Schmidt number, which are key parameters in commonly employed RANS solvers. The latter typically use isotropic formulations for the diffusivity, and in fact they perform poorly especially close to injection (Kohli & Bogard, 2005). The present calculation allows direct evaluation of the turbulent diffusivity in its natural tensorial form. Furthermore, deviation from the Reynolds analogy and the gradient-diffusion hypothesis can be examined.

NUMERICAL SET-UP

The flow configuration is depicted in Fig. 1. The simplified geometry includes the main geometrical and flow parameters relevant to gas turbine film cooling applications: the hole is inclined at an angle of 30° with respect to the main flow, and the hole length is about four times its diameter. The boundary layer thickness-to-hole diameter ratio is equal to one, as well as the velocity ratio. Density ratio and momentum flux ratio are also equal to one. Using the channel bulk velocity, the Reynolds number is $Re_D = 5,400$ based on the jet diameter D and $Re_d = 45,800$ based on the

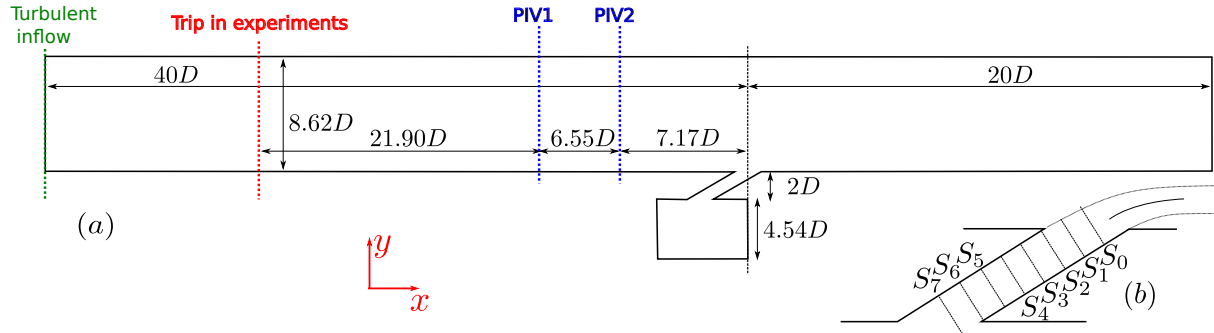


Figure 1. (a) Computational domain and PIV measurement planes. (b) Normal sections in the pipe used to plot velocity profiles in Fig. 2

duct height $d = 8.62D$.

Large eddy simulations are carried out with the massively parallel, finite-volume flow solver Charles^X developed at the Center for Turbulence Research. Although water is used in the experiment, the use of a compressible Navier-Stokes solver is motivated by the possibility to include compressibility effects in future studies. However, the regime under consideration is free from compressibility effects as the imposed Mach number is below 0.3. Moreover, in the present turbulent regime, the difference in molecular diffusivity between water, used in the experiments, and air, used in the simulation, is immaterial as turbulent diffusion is dominant. The transport equation of a passive scalar is considered in addition to the mass, momentum and total energy conservation equations. Sub-grid scale motions are accounted for with Vreman's eddy viscosity model (Vreman, 2004). The turbulent mixing at sub-grid scales is modeled using the Reynolds analogy between momentum and mass transfer, and a constant turbulent Schmidt number. We consider here a single grid, block-structured in all the regions of interest, with unstructured parts to coarsen the mesh close to the upper wall. The grid resolution is such that the first cell center is located at $y^+ < 1.5$ in all the walls, except the upper wall where a *slip* boundary condition is used, which is sufficient to capture the blockage effect. The grid includes 52 million control volumes to ensure high resolution of the turbulent structures. Note that a posteriori results shows that the sub-grid-scale viscosity/diffusivity is one order of magnitude smaller than the molecular viscosity/diffusivity in the regions of interest.

When a statistically steady state is reached, turbulent quantities are time-averaged over a period of 150 time units $T = D/U_\infty$.

INCOMING TURBULENT BOUNDARY LAYER

The turbulent inflow condition is specified using the synthetic method of turbulence generation proposed by Xie & Castro (2008) with the modifications of Touber & Sandham (2009), which is based on a digital filtering technique (Klein *et al.*, 2003). preliminary simulations in a simple rectangular duct are used to create a turbulent boundary layer with similar characteristics to the experimental profiles provided by the PIV measurements at locations PIV1 and PIV2 (see Fig. 1). Velocity and single-point-correlation profiles from PIV1 are rescaled with a 40% thick boundary layer to build the inflow conditions. Note that the Reynolds number had to be increased ($\times 1.8$) in compari-

son with experiments in order to trigger a turbulent state, but the momentum ratio was kept identical. Satisfactory agreement between simulated and measured inflow conditions was obtained with a development region extended to $40D \sim 40\delta^{PIV1}$. This is significantly higher than the $10 - 15\delta$ usually recommended for synthetic turbulence generation. This is attributed to the relatively low Reynolds number ($Re_\delta^{inflow} \sim 3000$) and induced large scale near-wall turbulent structures. Following this methodology, the generated inflow turbulence matches experimental single-point correlations at location PIV1 and PIV2 within experimental uncertainty, as shown by the comparison of the velocity profiles in Fig. 3a and Reynolds stresses in Fig. 3b. Boundary layer thickness growth is represented Fig. 4a, which shows consistent and comparable results with the experiments. A good indicator of the transition from synthetic to physical turbulence in a turbulent boundary layer is the shape factor or ratio between displacement and momentum thickness. Fig. 4b shows the slow evolution of the shape factor, which explains the need for a long upstream domain for the boundary layer to lose memory of the artificial inflow condition and develop in a physical manner. The interaction of the turbulent boundary layer with the jet can be visualized in the Fig. 5. This shows the importance of the interaction of turbulent structures in the crossflow boundary layer with the jet turbulence.

STRUCTURE AND DYNAMICS OF THE JET

A major interest of the present calculation lies in the complete representation of the jet inflow conditions. The plenum is fed laterally, although the inlet is not shown in Fig. 1a. This aspect, together with the asymmetric geometry of the plenum, produces a slight asymmetry in the jet inflow. This is well visualized in Fig. 2a where color contours of axial in-hole velocity are shown for several cross-sections of the pipe, both for the MRV measurements and for the LES calculations. The slight asymmetry is visible in the experimental data and is well captured by the simulations. In general the level of the agreement is excellent, as can be appreciated from the profiles extracted along the geometrical symmetry plane in Fig. 2b. The velocity pattern highlights the acceleration and separation at the inlet of the film cooling hole, resulting from the sharp angle between the plenum and the hole itself. This feature is crucial for the further development of the flow. The high shear, high velocity region adjacent to the separated zone is dynamically important especially in short-hole geometries like the present one, since

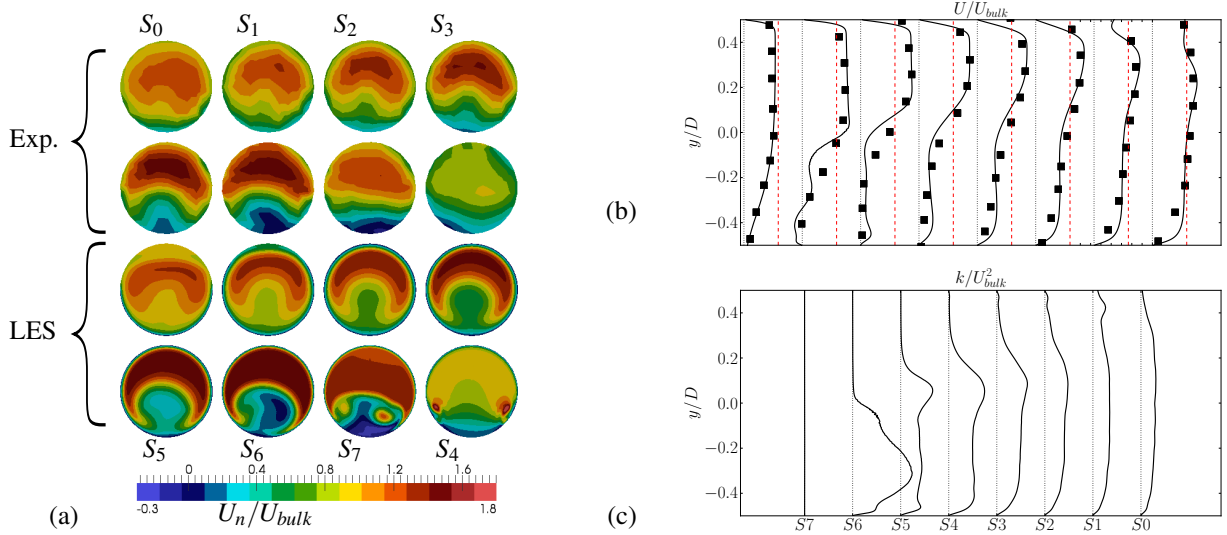


Figure 2. Flow field in the pipe. Comparison with experimental data (MRV). (a) 2D comparisons of the wall-parallel velocity field in wall-normal sections (locations specified in Fig. 1). Velocity (b) and turbulent kinetic energy profile (c) at the centerline of the circular sections. The red dashed line indicates the reference $U_{ref}/U_{bulk} = 1$.

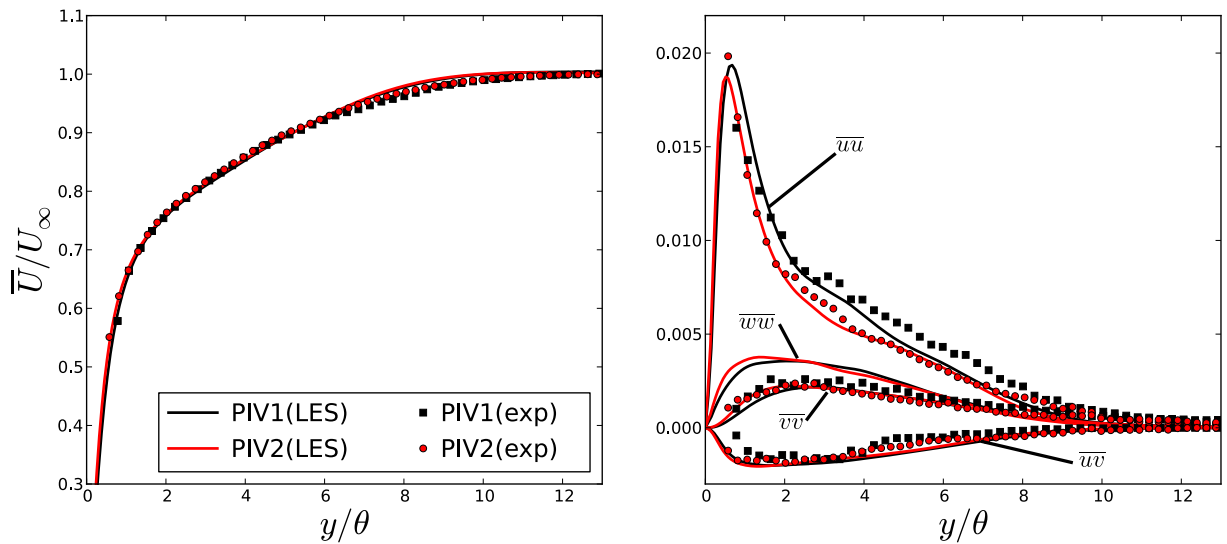


Figure 3. (a) Mean velocity and (b) Reynolds stress tensors profiles: comparison at location (PIV1) and (PIV2) with PIV data.

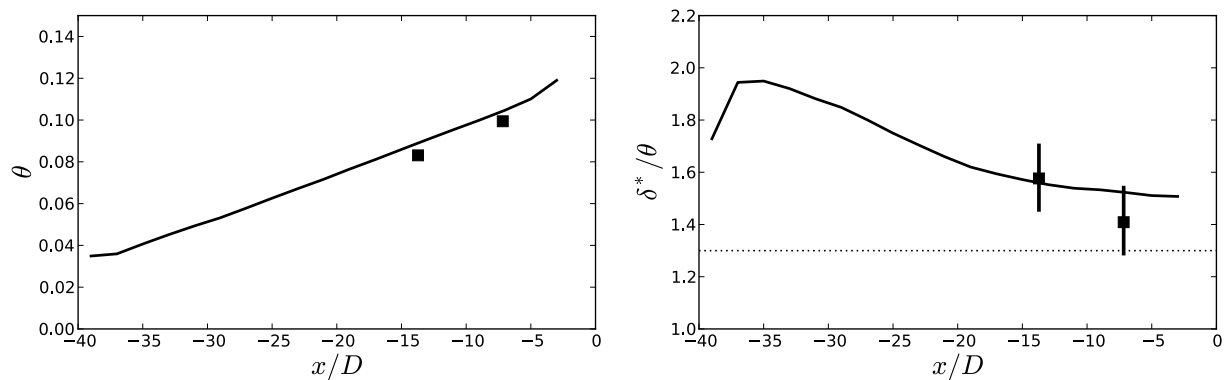


Figure 4. (a) Variation of momentum thickness and (b) shape factor of the turbulent boundary layer upstream of the interaction with the crossflow. Comparison with PIV measurements at two locations.

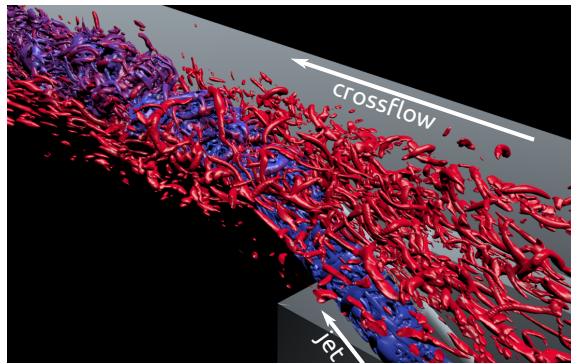


Figure 5. Concentration mapped on Q-criterion isosurfaces (red(0%) to blue (100%).

the flow does not have space to redevelop before interacting with the main flow. Also, counter-rotating vortices develop inside the hole, which might interact with the well known counter-rotating vortex pair (CVP) that characterize every jet in-crossflow.

The high shear produced by the separation at the entry of the hole corresponds to a peak in turbulent production, as highlighted by the profiles of turbulent kinetic energy in Fig. 2c. However the high level of agitation and stirring inside the hole acts to spread the turbulence intensity, which is almost homogeneous at the hole exit. Besides the effect on the mean quantities, the separation at the hole inlet also causes the quasi-periodic shedding of rings of azimuthal vorticity that can be observed in instantaneous realizations of the flow field. The specific shedding frequency depends on the local flow velocity and on the hole diameter, and therefore is expected to be of the same order of the shedding frequency of the hairpin vortices produced by the jet-crossflow interaction (Sau & Mahesh, 2008).

CONTAMINANT CONCENTRATION

Concentration of the passive scalar is time-averaged and compared with experimental data. The concentration is set to unity in the jet and zero in the crossflow. The molecular Schmidt number is set to unity. The agreement with the measurements is excellent, as supported by Fig. 6. Streamwise-normal (YZ) and wall-normal (XZ) cuts shows almost no deviation with the experiments, especially when one accounts for the voxel size used in the measurements and represented in Fig. 6. At the immediate exit of the jet, ($X = D$) we observed a noticeable difference with the experiments in the internal structure of the jet. The concentration contours show the footprint of the CVP, which seems to develop earlier in the experiments, as shown by the curved and inward pointing shape of high-level isocontours of scalar concentration. Differences in sharpness at the pipe exit could lead to such variability in the flow structure, however very small in comparison with the the voxel size of the measurements. Further downstream, the footprint of the counter-rotating vortex pair is easily seen in Fig. 6e. Size and intensity of the isocontours agrees very well with the experiments in this region (green/yellow curves), which is certainly a good indicator of that the of the CVP dynamics are correctly captured in the simulation. The envelope of the jet characterized with the lowest (10% and 30%), isocontours is very well captured by the numerical simulation from the jet exit to the end of the domain.

TURBULENT SCALAR FLUXES

The gradient diffusion model for the turbulent scalar fluxes is used in most RANS models, together with a Reynolds analogy which links momentum and scalar turbulent fluxes through a turbulent Schmidt number. However the two vectors, $\partial_i \bar{C}$ and $\overline{u_i c}$, are not necessarily aligned. In particular counter-gradient transport has been observed in several configurations, including jets in crossflow Muppidi & Mahesh (2007) or a simple asymmetric mixing layer (Beguier *et al.*, 1978). Such behavior, and more general mis-alignment between the scalar flux vector and the concentration gradient, has been attributed to large scale motions, which produce sudden engulfment of portions of fluid at different concentration. This results in a highly intermittent evolution of the scalar time-history, and calls for a distinction between small-scale mixing and large-scale stirring. However, in a single-point time-averaged perspective, the two mechanisms are indistinguishable. $\partial_i \bar{C}$ and $\overline{u_i c}$ can be extracted from the present LES simulation in order to explore the applicability of the gradient diffusion hypothesis. In the absence of any homogeneous directions, the level of convergence is satisfactory for the mean quantities of the main flow variables such as velocity, pressure or concentration. Regarding higher-order quantities such as $\overline{u_i c}$ and $\partial_i \bar{C}$, the fair level of convergence achieved allows a qualitative description of their trends. The comparison of $\overline{C u_i}$ and $\partial_i \bar{C}$ in the Fig. 7 shows that most of high-intensity scalar fluxes regions are associated with the high concentration-gradient regions located at the jet boundary, as well as in the symmetry plane $z = 0$, in which a local minimum of concentration appears under the influence of the CVP and triggers $\overline{u_2 c}$. However the alignment of the two vectors is generally poor: this can be highlighted by examining the streamwise component of the scalar fluxes. In particular, two striking features are noticed:

1. At the jet exit, a positive $\overline{C u_1}$ region immediately follows a negative $\overline{C u_1}$ region in a zone of positive $\partial_1 \bar{C}$. This behavior can be seen in the plane $y = 0.5D$ and with lower intensity in the plane $y = D$.
2. After $x = 5 - 6D$, the jet in its upper part ($y = D$), is characterized by a negative $\overline{C u_1}$ while the streamwise concentration gradient is almost negligible.

The first feature coincides with the region of intense shear-layer vortices and turbulent production peak. We note that engulfment of non-contaminated fluid can later lead to intermittent ejection of the unmixed part of this “captured” fluid and build a positive $\overline{C u_1}$. The same reasoning applies to the opposite event for contaminated fluid. However, further investigations are needed to clearly identify the origin of this transfer. Regarding the second feature, it should be first noticed that the intensity of the streamwise flux is of the same order of magnitude as the y and z components, leading to a consequent misalignment of the two vectors $\partial_i \bar{C}$ and $\overline{u_i c}$. Fig. 8 shows a scatter plot of each components of the two vectors. The gradient diffusion hypothesis seems remarkably well justified in the y and z directions, as the two quantities roughly follow a linear curve. However, it confirms that this does not apply to the x direction in which scalar fluxes are built, without correlation from the actual concentration gradient intensity. Possible explanation of this particular behavior can find its origin in the dynamics of the CVP. Indeed, large scale, intermittent motions dragging non-contaminated fluid inside the jet core would build such a scalar flux, without necessarily leaving a strong statistical

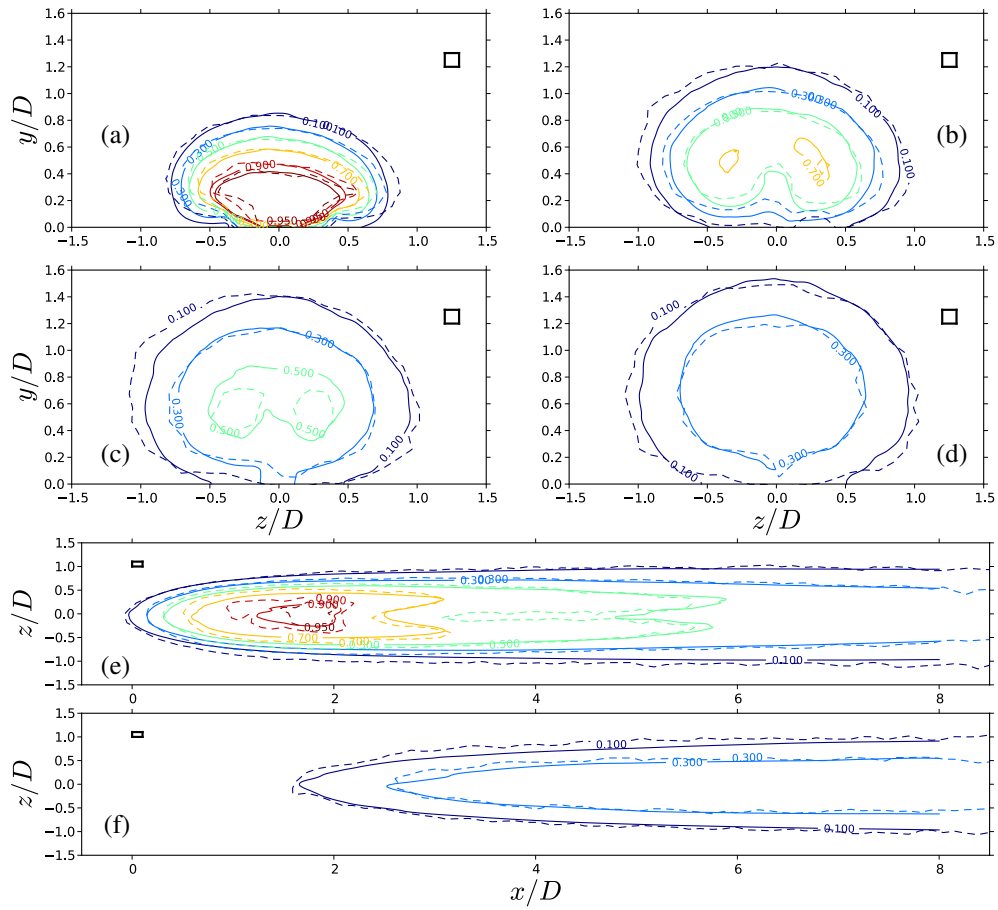


Figure 6. (a-b-c-d) Isocontours comparison of contaminant concentration between MRV data(dashed lines) and the present LES (solid lines) in YZ planes at $x = D - 3D - 5D - 7D$. (e,f) Same comparison in XZ planes at $y = 0.5D - D$. The black rectangle represents the size of a voxel in the experiments.

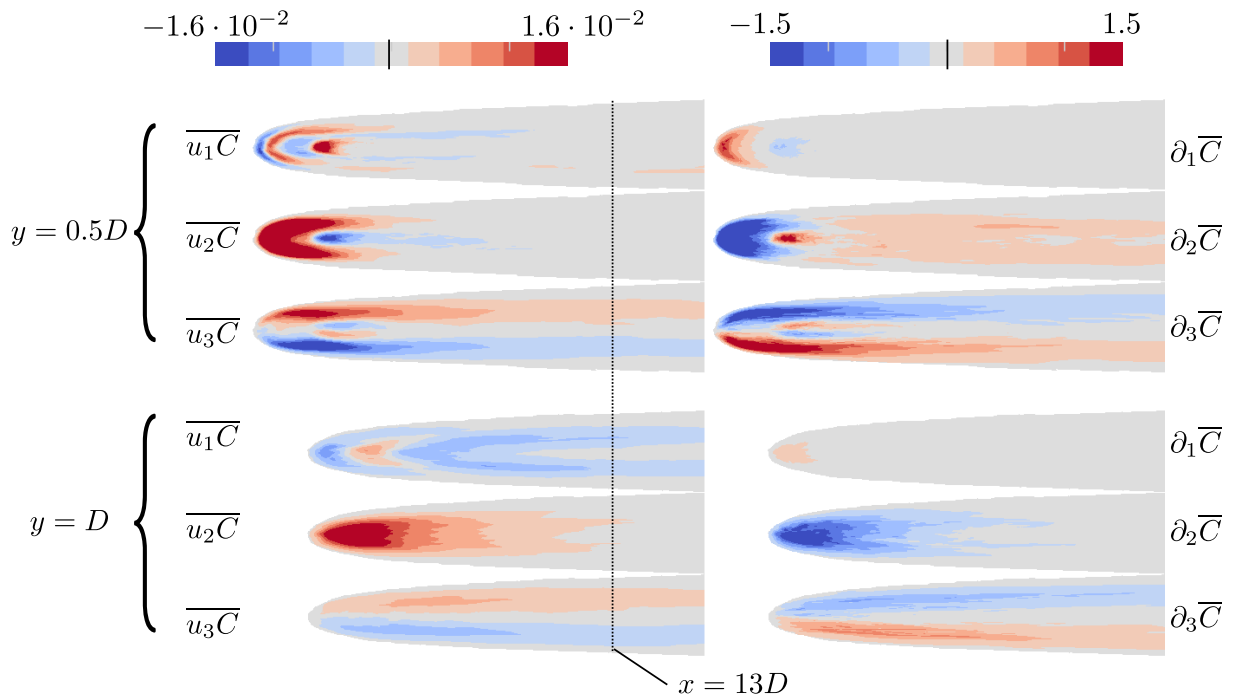


Figure 7. Scalar fluxes $\overline{u_i C}$ and $\partial_i \overline{C}$ in wall-normal planes. A threshold of $C = 0.005\%$ has been applied to extract the jet region.

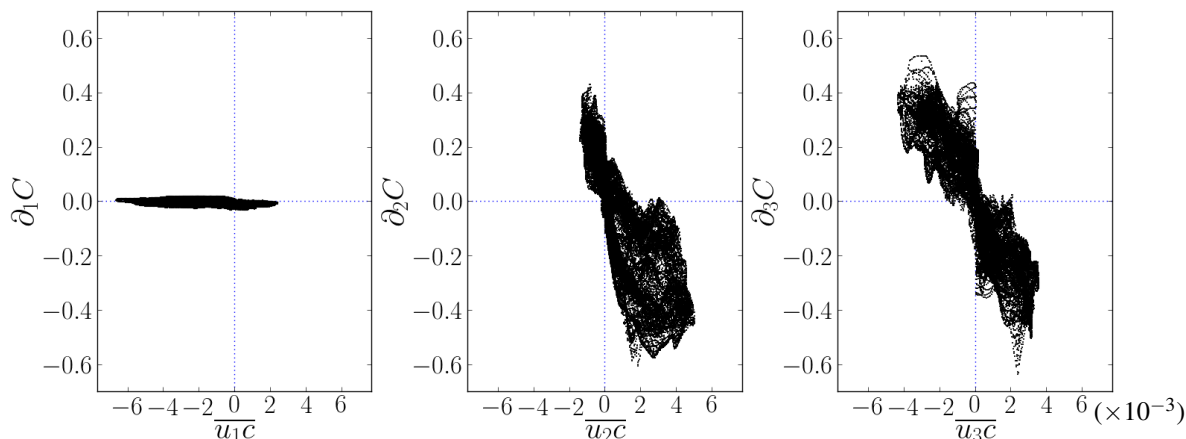


Figure 8. Scatter plot of $\partial_i C$ vs $u_i c$ in the plane $x = 13D$. Quantities are normalized using U_∞ , $C_{max} = 1$ and D .

footprint on the concentration gradient.

CONCLUSION

High-fidelity large eddy simulation of an inclined jet in crossflow has been performed and validated against experiments using the exact same geometry. The simulations were performed at a somewhat higher Reynolds number than the experiments, but with the same velocity ratio. The excellent agreement with the measurements shows that the discrepancy in Reynolds number does not affect the quantities of interest within the considered range. While the gradient diffusion hypothesis seems to hold for the wall-normal and spanwise directions, large misalignment between the turbulent scalar flux and the concentration gradient is found in the streamwise direction. It is hypothesized that this is linked to the large coherent structures in the jet, which produce intermittent and advective (rather than diffusive) transport. Further investigations of this assumption are ongoing.

ACKNOWLEDGEMENTS

Dr. Coletti was supported by a grant from Honeywell Corp. Computations have been performed on the *Vulcan* IBM Blue Gene/Q system at Lawrence Livermore National Laboratory, funded by the Advanced Simulation and Computing (ASC) Program of the National Nuclear Security Administration (NNSA). Access to *Vulcan* clusters was provided through the Predictive Science Academic Alliance Program (PSAAP) and is greatly acknowledged.

REFERENCES

- Acharya, Sumanta, Tyagi, Mayank & Hoda, Asif 2001 Flow and heat transfer predictions for film cooling. *Annals of the New York Academy of Sciences* **934** (1), 110–125.
- Beguier, Claude, Fulachier, Louis & Keffer, James F. 1978 The turbulent mixing layer with an asymmetrical distribution of temperature. *Journal of Fluid Mechanics* **89**, 561–587.
- Benson, M. J., Elkins, C. J., Mobley, P. D., Alley, M. T. & Eaton, J. K. 2010 Three-dimensional concentration

field measurements in a mixing layer using magnetic resonance imaging. *Experiments in Fluids* **49**, 43–55.

- Coletti, F., Elkins, C. & Eaton, J. 2012 An inclined jet in Cross-Flow studied by means of particle image velocimetry and magnetic resonance imaging .
- Elkins, C. J., Markl, M., Pelc, N. & Eaton, J. K. 2003 4D magnetic resonance velocimetry for mean velocity measurements in complex turbulent flows. *Experiments in Fluids* **34** (4), 494–503.
- Klein, M., Sadiki, A. & Janicka, J. 2003 A digital filter based generation of inflow data for spatially developing direct numerical or large eddy simulations. *Journal of Computational Physics* **186** (2), 652–665.
- Kohli, Atul & Bogard, David G. 2005 Turbulent transport in film cooling flows. *Journal of Heat Transfer* **127** (5), 513–520.
- Muldoon, Frank & Acharya, Sumanta 2009 DNS study of pulsed film cooling for enhanced cooling effectiveness. *International Journal of Heat and Mass Transfer* **52** (13–14), 3118–3127.
- Muppidi, Suman & Mahesh, Krishnan 2007 Direct numerical simulation of round turbulent jets in crossflow. *Journal of Fluid Mechanics* **574**, 59–84.
- Sau, Rajes & Mahesh, Krishnan 2008 Dynamics and mixing of vortex rings in crossflow. *Journal of Fluid Mechanics* **604**, 389–409.
- Touber, Emile & Sandham, Neil D. 2009 Large-eddy simulation of low-frequency unsteadiness in a turbulent shock-induced separation bubble. *Theoretical and Computational Fluid Dynamics* **23** (2), 79–107.
- Vreman, A. W. 2004 An eddy-viscosity subgrid-scale model for turbulent shear flow: Algebraic theory and applications. *Physics of Fluids* **16** (10), 3670–3681.
- Xie, Zheng-Tong & Castro, Ian P. 2008 Efficient generation of inflow conditions for large eddy simulation of Street-Scale flows. *Flow, Turbulence and Combustion* **81** (3), 449–470.
- Ziefle, Jörg & Kleiser, Leonhard 2008 Assessment of a film-cooling flow structure by large-eddy simulation. *Journal of Turbulence* pp. N29+.